RESEARCH

A wind semi-sub platform with hinged floats for omnidirectional swell wave energy conversion

Peter Stansby[1] · Gangqiang Li[1]

Abstract

The capacity of wind turbines on offshore wind platforms is presently much greater than that for wave energy conversion. However, wind availability with speed greater than 5 m/s, just above cut in, is typically 30–40% requiring storage to provide uniformity of supply, but this may be improved by adding swell wave energy conversion with typical availability of 90%. A hybrid platform is considered with three effectively rigid cylindrical floats connected by beams at right angles to support a wind turbine with its base on the central float, and two wave energy floats, opposite the wind floats, with beams at 90° and hinges with dampers for mechanical energy absorption on the central float. With swell periods over 10 s, pitch resonance may be achieved with the fore and aft floats about half a wavelength apart with anti-phase forcing causing a moment on hinges above water level. The NREL 5 MW wind turbine is incorporated and average swell wave power absorption in a typical significant wave height of 2 m is over 200 kW. The analysis is by time domain linear diffraction–radiation modelling validated for other multi-float configurations. Significant wave energy conversion is omnidirectional over a wide range of heading angles. An added benefit is that in larger waves associated with strong winds, when the wave energy conversion would be disengaged, the wave float rotation on free hinges reduces the hub accelerations below that for rigid floats, enabling a longer time for wind power generation.

Keywords Semi-sub wind platform · Hinged floats · Swell wave energy conversion · Linear modelling

1 Introduction

Massive exploitation of offshore wind energy is planned worldwide and much of this is in depths greater than 50 m requiring floating platforms. Various concepts are being developed with spar-type and semi-sub platforms already deployed successfully, e.g. Hywind and Windfloat, respectively. Tension leg platforms (TLPs) and barge-type platforms are also being considered. Present turbine capacities of around 5 MW are being extended to 12–15 MW and platforms for 20 MW are being designed (De Souza and Bachynski-Polić 2022). However, significant wind power requires speeds greater than about 5 m/s which has only 30–40% availability, e.g. Arinaga and Cheung (2012), which means that substantial storage is required for continuity of supply. On the other hand, swell wave power greater than 20 kW/m has availability typically of 90%, also Arinaga and Cheung (2012). Combining wave energy devices in wind farms has been assessed (Kluger et al. 2023) and shown to reduce the storage required. Wave energy devices may also be incorporated on wind semi-sub platforms directly, both to provide additional power output and potentially to reduce platform pitch motion. The wind turbine nacelle acceleration should be below about 0.3 g for drive train operation, e.g. Carbon Trust (2015). Platform motion is also a concern for on/off loading of equipment and personnel and is a general concern for human wellbeing.

Heaving point absorbers have been incorporated on a three-float semi-sub of Windfloat type (Roddier et al. 2010) between the upper and lower connecting beams (Hu et al. 2020). Analysis indicates average power of 300 kW is possible in regular waves with height 2 m. 6–15 wave floats were tested and the smaller number was optimal. In addition, the wave floats reduced pitch motion. Si et al. (2021) considered the three-float DeepCwind semi-sub (Robertson et al. 2017) with an additional hinged wave float outer to each float. In irregular waves with significant wave height $H_s = 2.5$ m and

✉ Peter Stansby
  p.k.stansby@manchester.ac.uk

[1] School of Engineering, University of Manchester, Manchester, UK

peak period $T_p = 10$ s, 180 kW mean wave power was generated with reactive control, although this increased platform motion while spring-damper control halved wave power, but slightly decreased platform motion. Kamarlouei et al. (2022) investigated experimentally a six-float semi-sub in a hexagonal formation and added three and six outer wave floats on three sides of the hexagon. The results are quite complex showing that wave floats affect platform motion, but optimisation is necessary to be effective. Michailides et al. (2016) investigated flap wave energy on a three-column semi-sub and estimated average power of 60 kW with $H_s = 3$ m and T_p in the range 7–12 s. A further concept with torus wave floats on the columns of a braceless three-float 5 MW wind platform was investigated numerically by Tian et al. (2023). In regular waves with height 2 m, four torus generated nearly 400 kW of mean wave power. However, pitch motions may be increased in swell waves and decreased in smaller wave periods. Li et al. (2018) investigated torus wave energy generation on a spar platform estimating 100 kW average power with $H_s = 2.3$ m and $T_p = 10$ s. Ren et al. (2020) also investigated torus wave energy generation on a TLP giving 800 kW with $H_s = 6$ m and $T_p = 11$ s.

Platform motion may be reduced directly in semi-subs by allowing water to oscillate internally between floats as tuned mass dampers in resonance, e.g. Fath et al. (2020), or by actively pumping between floats (Stansby 2021). The latter reduces motion by 30–50% by balancing heave-induced forces in floats with relatively small power requirements as the pumps can also operate as turbines, so the net power required has only to overcome friction losses in the connecting pipes.

In this paper, we consider further the addition of hinged wave floats to generate power from swell waves which are generally present even when the regional wind speed is small, below the cut-in value for a wind turbine. When wind speed is above rated, wave power will be small relative to wind and not necessary. The wave floats are integrated with the wind floats to be aligned and of the same size. Wave power should be significant for a wide range of headings. The fore-aft spacing of wind to wave floats should enable forcing to be roughly in anti-phase to generate moment due to surge forcing about the hinges above the deck level. A further aim is to reduce pitch and roll on the wind floats and hence acceleration at the hub. The analysis is by time domain linear diffraction–radiation modelling, validated previously for multi-float wave energy configurations (Stansby et al. 2017; Stansby and Carpintero Moreno 2020), shown experimentally to be remarkably linear even in large waves (Santo et al. 2017; Stansby and Carpintero Moreno 2020).

The paper is organised as follows. The next section describes the idealised platform to support an NREL 5 MW turbine, e.g. Robertson et al. (2017). The hydrodynamic modelling Sect. 3 follows, based on a time domain linear
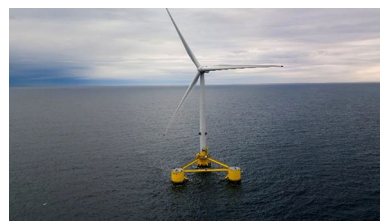

Fig. 1 Windfloat platform, photo of the Kincardine Offshore Wind Farm project courtesy of Principle Power
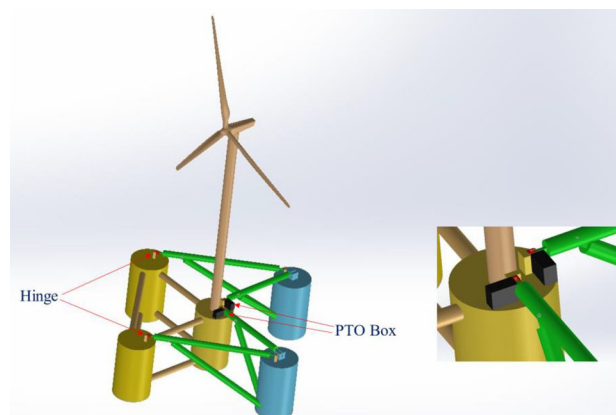

Fig. 2 Diagrammatic sketch of hybrid wind–wave platform. The yellow floats are rigidly connected to support the wind turbine. The blue floats are connected to the wind floats by green beams which rotate the power take-off (PTO) on hinges. On the mid-float hinges, PTO boxes are incorporated for wave energy conversion, shown enlarged in the inset

wave–platform interaction model of Cummins form including the actuator torques and float drag. This is developed from an in-house code applied to the multi-float wave energy converter M4 showing good agreement with experiment, as reviewed in Stansby and Draycott (2024). Section 4 describes the results for various wave and wind conditions. Waves with headings between 0° and 360° are analysed. The results are discussed in Sect. 5 and conclusions follow.

2 Platform design

We consider a three float wind platform similar to WindFloat (Fig. 1) except the angle between the floats outer to the float supporting the turbine is 90°. This is so that two additional floats may be located opposite the outer floats with hinges on the central supporting float as shown in Fig. 2. These float positions rotate principally in vertical planes and damping torque is applied at the hinges to absorb mechanical energy.

To test this concept, we use the well-known 5 MW NREL turbine (Robertson et al. 2017) and all floats are of 15 m diameter and 15.7 m draft. This provides sufficient buoyancy to support the turbine. The hinged floats are effectively free

Table 1 BEM mode notation

Body i	Mode number	Symbol
Surge	$1 + 6(i - 1)$	H
Sway	$2 + 6(i - 1)$	T
Heave	$3 + 6(i - 1)$	V
Roll	$4 + 6(i - 1)$	M_x
Pitch	$5 + 6(i - 1)$	M_y

floating with axes vertical in still water. The effective mass distribution is given in Table 1 incorporating the masses of cross beams. The buoyancy of each float is 2774e3 kg. This is an idealised platform specified to demonstrate the concept. The hinge point for floats 4 and 5 is 10 m above SWL and freeboard is 9 m. Higher hinge points were not found to increase power. The spacing between outer floats and mid float 2 is 40 m. These dimensions are similar to those of DeepCwind.
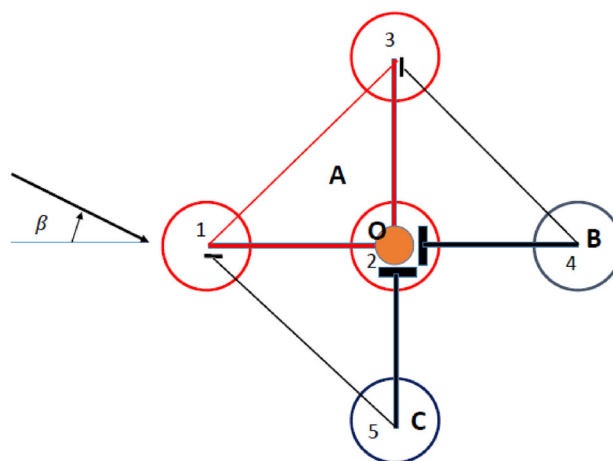

Fig. 3 Plan view of configuration with wind support body A (in red) and stabilising hinged wave floats B and C (in black) with hinges/PTO at right angles at O shown as thick solid lines. Principal beams are shown as thick lines and secondary beams as thin lines. The turbine column on A is solid orange. β is the heading angle.

Float number	Float		Ballast		Turbine + column (OC5)	
	Mass (kg)	Position relative to SWL (m)	Mass (kg)	Position relative to SWL (m)	Mass (kg)	position relative to SWL (m)
1	1500e3	− 2.85	1274e3	− 12.56		
2	1500e3	− 2.85	236e3	− 14.13	1038e3	67.5
3	1500e3	− 2.85	1274e3	− 12.56		
4	1500e3	− 2.85	1274e3	− 12.56		
5	1500e3	− 2.85	1274e3	− 12.56		−

The centre of mass of combined floats A (123) is 0.15 m above SWL, while the centre of buoyancy is − 7.85 m

3 Mathematical formulation and model

In the multi-float time-domain formulation, hydrodynamic forces are due to linear wave excitation including diffraction, added mass, radiation damping, restoring, drag and wind forces. Their definitions are based on hydrodynamic frequency-domain potential-flow coefficients from the BEM OREGEN code (Li and Stansby 2023) in Cummins method for irregular waves. The standard form of the JONSWAP wave spectrum will be used with a high spectral peakedness $\gamma = 3.3$ representative of swell waves. Five degrees of freedom are included with yaw assumed to be negligible due to mooring constraint.

Angular rotations about the y axis θ_y and the x axis θ_x through O are clockwise positive, h is the horizontal longitudinal distance from O to a float mid-point, t is the transverse distance from O, and v is the vertical distance from O, positive downwards. H, V and T are total hydrodynamic forces in conventional x, z, y directions, M_y is pitch moment and M_x is roll moment about O.

Although there are three A floats, these may be considered as a single body ($n_A = 3$ floats) with hinged float B ($n_B = 1$) and float C ($n_c = 1$) acting individually in Fig. 3. The total number of floats $N = n_A + n_B + n_C = 5$. Note the mooring constraint will be applied as a small horizontal stiffness forces in two directions to prevent drift.

Bodies A and C are effectively combined in pitch and $\Sigma^{n_{AC}}$ denotes summation for bodies A and C. Taking moments about the y axis at O for pitch accounting for masses (turbine, floats, ballast),

$$-\sum_{i=1}^{n_{AC}} m_i v_i \ddot{x}_i - \sum_{i=1}^{n_{AC}} m_i h_i \ddot{z}_i + I_{AC}\ddot{\theta}_y$$
$$= M_{\text{mech},\,y} + M_{\text{wind},\,y} + \sum_{i=1}^{n_{AC}} M_{y,\,i} - \sum_{i=1}^{n_{AC}} h_i V_i - \sum_{i=1}^{n_{AC}} v_i H_i. \tag{1}$$

I is moment of inertia about the centre of mass for A and C and $I_{AC} = I_A + I_C$, $M_{\text{mech},\,y}$ is moment due to mechanical damping (PTO) about the y axis at O and $M_{\text{wind},\,y}$ is the moment due to wind thrust $H_{\text{wind},\,x}$ defined below.

For B, with $i = 1$, taking moments about O as the float responds individually:

$$-m_i v_i \ddot{x}_i - m_i h_i \ddot{z}_i + I_i \ddot{\theta}_{y,\,i} = -M_{\text{mech},\,y} + M_{y,\,i} - h_i V_i - v_i H_i \tag{2}$$

where $M_{\text{mech},\,y} = -B_{\text{mech}}\dot{\theta}_{r,\,y}$, and $\theta_{r,\,y} = \theta_{y,\,AC} - \theta_{y,\,i}$.

Bodies A and B are effectively combined in roll. Taking moments about x axis at O:

$$\sum_{i=1}^{n_{AB}} m_i v_i \ddot{y}_i + \sum_{i=1}^{n_{AB}} m_i t_i \ddot{z}_i + I_{AB}\ddot{\theta}_x$$
$$= M_{\text{mech},\,x} + \sum_{i=1}^{n_{AB}} M_{x,\,i} + \sum_{i=1}^{n_{AB}} t_i V_i + \sum_{i=1}^{n_{AB}} v_i T_i, \tag{3}$$

where $I_{AB} = I_A + I_B$, and $M_{\text{mech},\,x}$ is moment due to mechanical damping about the x axis at O. Wind thrust in this direction is not considered here.

For C, with $i = 1$, taking moments about O as the float responds individually:

$$m_i v_i \ddot{y}_i + m_i t_i \ddot{z}_i + I_i \ddot{\theta}_{x,\,i} = -M_{\text{mech},\,x} + M_{x,\,i} + t_i V_i + v_i H_i, \tag{4}$$

where $M_{\text{mech},\,x} = -B_{\text{mech}}\dot{\theta}_{r,\,x}$, and $\theta_{r,\,x} = \theta_{x,\,AB} - \theta_{x,\,i}$,
for the whole system as there is no net force or net moment on a hinge.

In the longitudinal horizontal direction (for all masses),

$$\sum_{i=1}^{N} m_i \ddot{x}_i = \sum_{i=1}^{N} H_i + H_{\text{wind},\,x} + H_{\text{stiff}}, \tag{5}$$

where stiffness force $H_{\text{stiff}} = -k_s x_O$ and k_s is the elastic constant.

In the transverse horizontal direction,

$$\sum_{i=1}^{N} m_i \ddot{y}_i = \sum_{i=1}^{N} T_i + T_{\text{stiff}}, \tag{6}$$

where stiffness force $T_{\text{stiff}} = -k_s y_O$.

In the vertical direction,

$$\sum_{i=1}^{N} m_i \ddot{z}_i = \sum_{i=1}^{N} V_i. \tag{7}$$

The positions of the centres of gravity of each float x_i, z_i, y_i in relation to O, linearised for small angles, are defined by:

For all floats, $i = 1$, N

$$x_i = x_O + h_i - v_i \theta_y, \tag{8a}$$

$$z_i = z_O - v_i - h_i \theta_y + t_i \theta_x, \tag{8b}$$

$$y_i = y_O + t_i + v_i \theta_x. \tag{8c}$$

We thus have seven equations for seven unknowns x_O, y_O, z_O, $\theta_{y,\,A}$, $\theta_{y,\,B}$, $\theta_{x,\,A}$, $\theta_{x,\,C}$.

For AC in pitch:

$$-\sum_{i=1}^{n_{AC}} m_i v_i \left(\ddot{x}_O - v_i \ddot{\theta}_y\right) - \sum_{i=1}^{n_{AC}} m_i h_i \left(\ddot{z}_O - h_i \ddot{\theta}_{yA} + t_i \ddot{\theta}_x\right)$$
$$+ I_{AC}\ddot{\theta}_y = M_{\text{mech},\,y} + M_{\text{wind},\,y}$$
$$+ \sum_{i=1}^{n_{AB}} M_{y,\,i} - \sum_{i=1}^{n_{AB}} h_i V_i - \sum_{i=1}^{n_{AB}} v_i H_i, \tag{9}$$

giving

$$\ddot{\theta}_y \left(\sum_{i=1}^{n_{AC}} m_i v_i^2 + \sum_{i=1}^{n_{AC}} m_i h_i^2 + I_{AC}\right)$$
$$= \sum_{i=1}^{n_{AC}} m_i v_i \ddot{x}_O + \sum_{i=1}^{n_{AC}} m_i h_i \ddot{z}_O + M_{\text{mech},\,y} + M_{\text{wind},\,y}$$
$$+ \sum_{i=1}^{n_{AC}} M_{y,\,i} - \sum_{i=1}^{n_{AC}} h_i V_i - \sum_{i=1}^{n_{AC}} v_i H_i + \sum_{i=1}^{n_{AC}} m_i h_i t_i \ddot{\theta}_x, \tag{10}$$

and for B float $i = 1$,

$$-m_i v_i \left(\ddot{x}_O - v_i \ddot{\theta}_{y,\,i}\right) - m_i h_i \left(\ddot{z}_O - h_i \ddot{\theta}_{y,\,i} + t_i \ddot{\theta}_x\right)$$
$$+ I_{y,\,i}\ddot{\theta}_{y,\,i} = -M_{\text{mech}y} + M_{y,\,i} - h_i V_i - v_i H_i, \tag{11}$$

giving

$$\ddot{\theta}_{y,\,i} \left(m_i v_i^2 + m_i h_i^2 + I_{y,\,i}\right) = m_i v_i \ddot{x}_O + m_i h_i \ddot{z}_O$$
$$+ m_i h_i t_i \ddot{\theta}_{x,\,i} - M_{\text{mech}y}$$
$$+ M_{y,\,i} - h_i V_i - v_i H_i. \tag{12}$$

For AB in roll:

$$\sum_{i=1}^{n_{AB}} m_i v_i \left(\ddot{y}_O + v_i \ddot{\theta}_x \right) + \sum_{i=1}^{n_{AB}} m_i t_i \left(\ddot{z}_O - h_i \ddot{\theta}_y + t_i \ddot{\theta}_x \right)$$
$$+ I_{AB} \ddot{\theta}_x = M_{\mathrm{mech},x} + \sum_{i=1}^{n_{AB}} M_{x,i} + \sum_{i=1}^{n_{AB}} t_i V_i + \sum_{i=1}^{n_{AB}} v_i T_i, \tag{13}$$

giving

$$\ddot{\theta}_x \left(\sum_{i=1}^{n_{AB}} m_i v_i^2 + \sum_{i=1}^{n_{AB}} m_i t_i^2 + I_{AB} \right)$$
$$= -\sum_{i=1}^{n_{AB}} m_i v_i \ddot{y}_O - \sum_{i=1}^{n_{AB}} m_i t_i \ddot{z}_O + M_{\mathrm{mech},x}$$
$$+ \sum_{i=1}^{n_{AB}} M_{x,i} + \sum_{i=1}^{n_{AB}} t_i V_i + \sum_{i=1}^{n_{AB}} v_i T_i + \sum_{i=1}^{n_{AB}} m_i h_i t_i \ddot{\theta}_y. \tag{14}$$

For C float $i = 1$,

$$m_i v_i \left(\ddot{y}_O + v_i \ddot{\theta}_{x,i} \right) + m_i t_i \left(\ddot{z}_O - h_i \ddot{\theta}_{x,i} + t_i \ddot{\theta}_x \right) + I_{x,i} \ddot{\theta}_{x,i}$$
$$= -M_{\mathrm{mech},x} + M_{x,i} + t_i V_i + v_i H_i, \tag{15}$$

giving

$$\ddot{\theta}_{x,i} \left(m_i v_i^2 + m_i t_i^2 + I_{x,i} \right) = -m_i v_i \ddot{y}_O - m_i t_i \ddot{z}_O + m_i h_i t_i \ddot{\theta}_{x,i}$$
$$- M_{\mathrm{mech},x} + M_{x,i} + t_i V_i + v_i H_i. \tag{16}$$

For the whole system in the horizontal longitudinal direction,

$$\sum_{i=1}^{N} m_i \left(\ddot{x}_O - v_i \ddot{\theta}_{y,i} \right) = \sum_{i=1}^{N} H_i + H_{\mathrm{wind},x} + H_{\mathrm{stiff}}, \tag{17}$$

giving

$$\ddot{x}_O \sum_{i=1}^{N} m_i = \sum_{i=1}^{N} H_i + H_{\mathrm{wind},x} + H_{\mathrm{stiff}} + \sum_{i=1}^{N} m_i v_i \ddot{\theta}_{y,i}; \tag{18}$$

in the transverse direction,

$$\sum_{i=1}^{N} m_i \left(\ddot{y}_O + v_i \ddot{\theta}_{x,i} \right) = \sum_{i=1}^{N} T_i + T_{\mathrm{stiff}}, \tag{19}$$

giving

$$\ddot{y}_O \sum_{i=1}^{N} m_i = \sum_{i=1}^{N} T_i + T_{\mathrm{stiff}} - \sum_{i=1}^{N} m_i v_i \ddot{\theta}_{x,i} \tag{20}$$

and in the vertical

$$\sum_{i=1}^{N} m_i \left(\ddot{z}_O - h_i \ddot{\theta}_{y,i} + t_i \ddot{\theta}_{x,i} \right) = \sum_{i=1}^{N} V_i, \tag{21}$$

giving

$$\ddot{z}_O \sum_{i=1}^{N} m_i = \sum_{i=1}^{N} V_i + \sum_{i=1}^{N} m_i h_i \ddot{\theta}_{y,i} - m_i t_i \ddot{\theta}_{x,i}. \tag{22}$$

We thus have equations for $\ddot{\theta}_{y,AC}$, $\ddot{\theta}_{x,AB}$, $\ddot{\theta}_{y,B}$, $\ddot{\theta}_{y,C}$, $\ddot{x}_O$, $\ddot{y}_O$, $\ddot{z}_O$ which are further complicated by H_i, T_i, V_i, $M_{y,i}$, $M_{x,i}$ defined below also being a function of these variables and hydrodynamic (BEM) coefficients.

We are concerned with irregular waves with surface elevation $\eta(t)$, which will be defined by linear superimposition of K components of amplitude a_k, frequency $f = k\Delta f$, and random phase $\varphi_{r,k}$, where $k = 1$, K and Δf is frequency increment, such that

$$\eta(t) = \sum_{k=1}^{K} a_k \cos(-k 2\pi \Delta f t + \varphi_{r,k}), \tag{23}$$

specified in Sect. 5.

Hydrodynamic moments and forces are defined using conventional notation as shown in Table 1.

Linear diffraction forces and moments for each float are defined by frequency-dependent BEM coefficients for force/moment amplitude F and phase φ, or real and imaginary parts, but the former is more convenient as there is already a random phase for each frequency component. For each float $i = 1$, N-Pitch moment:

$$M_{y,D\ 5+6(i-1)} = \sum_{k=1}^{K} a_k F_{5+6(i-1),k} \cos\left(-k 2\pi \Delta f t + \varphi_{5+6(i-1),k} + \varphi_{r,k}\right). \tag{24a}$$

Roll moment:

$$M_{x,D\ 4+6(i-1)} = \sum_{k=1}^{K} a_k F_{4+6(i-1),k} \cos\left(-k 2\pi \Delta f t + \varphi_{4+6(i-1),k} + \varphi_{r,k}\right). \tag{24b}$$

Vertical force:

$$V_{D\ 3+6(i-1)} = \sum_{k=1}^{K} a_k F_{3+6(i-1),k} \cos\left(-k 2\pi \Delta f t + \varphi_{3+6(i-1),k} + \varphi_{r,k}\right). \tag{24c}$$

Longitudinal horizontal force:

$$H_{D\ 1+6(i-1)} = \sum_{k=1}^{K} a_k F_{1+6(i-1),\,k} \cos\left(-k2\pi\Delta f t + \varphi_{1+6(i-1),\,k} + \varphi_{r,\,k}\right). \tag{24d}$$

Transverse horizontal force:

$$T_{D\ 2+6(i-1)} = \sum_{k=1}^{K} a_k F_{2+6(i-1),\,k} \cos\left(-k2\pi\Delta f t + \varphi_{2+6(i-1),\,k} + \varphi_{r,\,k}\right). \tag{24e}$$

Added mass and radiation damping forces and moments are defined by frequency-dependent coefficients A and B, respectively, using the Cummins method. With a single body and one degree of freedom x we have

$$m\ddot{x}(t) = f(t) - A^{\infty}\ddot{x}(t) - \int_{-\infty}^{t} L(t-\tau)\dot{x}(\tau)\mathrm{d}\tau, \tag{25}$$

where f includes forces due to excitation, restoring and PTO; A^{∞} is added mass for infinite frequency and the impulse response function for radiation damping is given by

$$L(t) = \frac{2}{\pi} \int_{0}^{\infty} B(\omega)\cos(\omega t)\mathrm{d}\omega. \tag{26}$$

In discrete form with time step Δt, time $t = n\Delta t$ and $\omega = 2\pi f = k\Delta\omega$,

$$L^m = \frac{2}{\pi} \sum_{k=0}^{K} B_k \cos(k\Delta\omega n\Delta t)\Delta\omega, \tag{27}$$

which is precomputed and in discrete form

$$-\int_{-\infty}^{t} L(t-\tau)\dot{x}(\tau)\mathrm{d}\tau = - \sum_{l=n-2\mathcal{M}}^{n} L^{n-l} \dot{x}^l \Delta\tau, \tag{28}$$

where $\Delta\tau = \Delta t$ and $\mathcal{M} = T_{\mathrm{p}}/\Delta t$. The lower limit $(m - 2\mathcal{M})$ is generally used to represent $-\infty$ with almost identical results given by $(m - 4\mathcal{M})$.

The RHS is generalised for each float with six modes. For each float $i = 1$, N pitch moments are defined by:

$$M_{y,i} = M_{D\ 5+6(i-1)} - \sum_{j=1}^{n} A^{\infty}_{5+6(i-1),\,5+6(j-1)} \cdot \ddot{\theta}_j$$

$$- \sum_{j=1}^{n} \int_{-\infty}^{t} L_{5+6(i-1),\,5+6(j-1)} (t-\tau)\dot{\theta}_j(\tau)\mathrm{d}\tau$$

$$- \sum_{j=1}^{n} A^{\infty}_{5+6(i-1),\,4+6(j-1)} \cdot \ddot{\theta}_{Rj}$$

$$- \sum_{j=1}^{n} \int_{-\infty}^{t} L_{5+6(i-1),\,4+6(j-1)} (t-\tau)\dot{\theta}_{Rj}(\tau)\mathrm{d}\tau$$

$$- \sum_{j=1}^{n} A^{\infty}_{5+6(i-1),\,1+6(j-1)} \cdot \ddot{x}_j$$

$$- \sum_{j=1}^{n} \int_{-\infty}^{t} L_{5+6(i-1),\,1+6(j-1)} (t-\tau)\dot{x}_j(\tau)\mathrm{d}\tau$$

$$- \sum_{j=1}^{n} A^{\infty}_{5+6(i-1),\,3+6(j-1)} \cdot \ddot{z}_j$$

$$- \sum_{j=1}^{n} \int_{-\infty}^{t} L_{5+6(i-1),\,3+6(j-1)} (t-\tau)\dot{z}_j\mathrm{d}\tau$$

$$- \sum_{j=1}^{n} A^{\infty}_{5+6(i-1),\,2+6(j-1)} \cdot \ddot{y}_j$$

$$- \sum_{j=1}^{n} \int_{-\infty}^{t} L_{5+6(i-1),\,2+6(j-1)} (t-\tau)\dot{y}_j\mathrm{d}\tau$$

$$+ M_{y,\mathrm{rest}i}, \tag{29}$$

where the subscripts rest indicate restoring moments to be described below.

As an example, the discrete form of the term

$$- \sum_{j=1}^{n} \int_{-\infty}^{t} L_{5+6(i-1),\,5+6(j-1)} (t-\tau)\dot{\theta}_j(\tau)\mathrm{d}\tau$$

$$= - \sum_{j=1}^{n} \sum_{l=m-2\mathcal{M}}^{m} L^{m-l}_{5+6(i-1),\,5+6(j-1)} \dot{\theta}_j^l \Delta t.$$

There are equivalent terms for roll, heave, surge and sway; for heave, surge and sway there are additional terms for drag: $V_{\mathrm{drag}\,i}$, $H_{\mathrm{drag}\,i}$, $T_{\mathrm{drag}\,i}$, defined below, e.g. Stansby et al. (2017).

The restoring heave force for a single float $V_{\mathrm{rest},i} = -\rho g \pi r^2 z_i$. The restoring pitch and roll moments for floats are given by $M_{y,\mathrm{rest},1235} = 7.48e8\theta_y$, $M_{x,\mathrm{rest},1234} = 7.48e8\theta_x$, (both acting on 4 floats) $M_{y,\mathrm{rest},4} = -\rho g \pi \frac{r^4}{4}\theta_y$, $M_{x,\mathrm{rest},5} = -\rho g \pi \frac{r^4}{4}\theta_x$, where r is float radius ($H_{\mathrm{rest}} = T_{\mathrm{rest}} = 0$). The hydrostatic rotation effect is included for all floats. For floats 4 and 5, this is the only effect as centre of buoyancy and mass are assumed coincident, but they are not for 1235 and 1234 causing positive values. The drag forces are given by $H_{\mathrm{drag}\,i} = -0.5\rho A_i C_D |\dot{x}_i|\dot{x}_i$, $T_{\mathrm{drag}\,i} = -0.5\rho A_i |\dot{y}_1|\dot{y}_1$, $V_{\mathrm{drag}i} = -0.5\rho\pi r_i^2 C_D |\dot{z}_1|\dot{z}_1$. A_i is the vertical submerged frontal area for a float. Note float velocity relative to flow velocity is not considered and drag coefficient C_D is generally unity in this study.

The equations were advanced in time using the explicit Beeman's method for $\theta_{y,AC}$, $\theta_{y,B}$, $\theta_{x,AB}$, $\theta_{x,C}$, x_O, y_O, z_O

with time step Δt for general variable f

$$f^{n+1} = f^n + \dot{f}^n \Delta t + \ddot{f}^n \Delta t^2/2, \tag{30a}$$

$$\dot{f}^{n+1} = \dot{f}^n + \ddot{f}^n \Delta t. \tag{30b}$$

The BEM coefficients are for all cross coupled terms between floats as well as for the directly coupled (diagonal) terms which have the greatest magnitude. There are thus $(5N)^2$ non-zero coefficients for N floats with five modes here (heave, surge, sway, pitch and roll) for radiation damping and added mass and with $5N$ coefficients for diffraction forces. Forming a direct formulation for each term with all cross coupled terms would be tedious to generalise.

However, the dominant diagonal terms in added mass for each of $\ddot{\theta}_{y,AC}, \ddot{\theta}_{y,B}, \ddot{\theta}_{x,AB}, \ddot{\theta}_{x,C}, \ddot{x}_O, \ddot{y}_O, \ddot{z}_O$ may be removed from the RHS of each of H_i, $T_i V_i$, $M_{x,i}$, $M_{y,i}$ and added to the LHS of Eqs. (10), (12), (14), and (16). This proved desirable for numerical stability. An iteration is required with updated values of accelerations $\ddot{\theta}_A$, $\ddot{\theta}_B$, $\ddot{\theta}_R$, $\ddot{x}_O$, $\ddot{z}_O$ for terms on the RHS, but this showed fast convergence with less than ten iterations (default value). The radiation damping and diffraction force terms were not modified in the iteration. A time step size of $T_p/200$ was sufficiently small to give converged results (to plotting accuracy).

The equation set with numerical solution is thus complete and proved stable and convergent.

4 Linear damper and wind thrust

For wave energy conversion, the torques are passive linear dampers such that

$$M_{\text{mech},y} = -B_{\text{mech}}\dot{\theta}_{y,r}, \tag{31a}$$

$$M_{\text{mech},x} = -B_{\text{mech}}\dot{\theta}_{x,r}, \tag{31b}$$

where B_{mech} is the linear damping constant, $\dot{\theta}_{y,r} = \dot{\theta}_{y,AC} - \dot{\theta}_{y,B}$ and $\dot{\theta}_{x,r} = \dot{\theta}_{x,AB} - \dot{\theta}_{y,C}$.

Mechanical power is given by

$$P_{\text{mech}} = B_{\text{mech}}\dot{\theta}_{y,r}^2 + B_{\text{mech}}\dot{\theta}_{x,r}^2. \tag{32}$$

The unsteady wind thrust in the x direction is given by

$$H_{\text{wind},x} = 0.5\rho_{\text{air}} A_{\text{turb}} C_T (U_{\text{hub}} - \dot{x}_{\text{hub}})^2, \tag{33}$$

where U_{hub} is the uniform wind speed at the hub, $\dot{x}_{\text{hub}}$ is the hub velocity, ρ_{air} is the air density (1.2 kg/m^3) and A_{turb} is the swept area for the rotor of radius r_{turb}, πr_{turb}^2. The thrust coefficient C_T is dependent on the wind speed and is

determined from blade element momentum theory (BEMT) using the NREL 5 MW turbine characteristics. The force is assumed to be quasi steady and defined by the relative velocity ($U_{\text{hub}} - \dot{x}_{\text{hub}}$). The quasi-steady behaviour has been shown to be a close approximation to CFD modelling using the actuator line model (Apsley and Stansby 2020). The moment $M_{\text{wind},y} = v_{\text{hub}} H_{\text{wind},x}$ where v_{hub} is the height of the hub above hinge O.

5 Wave conditions

We specify irregular waves by the standard JONSWAP spectrum $S(f)$ defined by a significant wave height H_s and a peak frequency $f_p = 1/T_p$, where T_p is the peak period; a spectral peakedness factor $\gamma = 3.3$ was applied. The surface elevation η at O may be defined by linear superposition of the discretised wave amplitude components as given by Eq. 23. The lower limit on frequency was 0.032 Hz (0.2 rad/s) and the upper limit 0.318 Hz (2.0 rad/s), between two and four times f_p, $\Delta f = 0.00159$ Hz (0.01 rad/s) giving 181 frequency components with amplitude $a_k = \sqrt{2S(f)\Delta f}$, and φ_r is the phase from a uniform random distribution between 0 and 2π. This defines the frequencies for which the BEM coefficients are computed. The frequency increment, however, determines the repeat times which would be 629 s (approximately 10 min) while run times are required to be typically 3600 s (1 h). A frequency increment $\Delta f_{\text{rt}} = 1/t_{\text{rt}}$ would give the run time t_{rt} as a repeat time and the associated spectrum is obtained by interpolation within a frequency increment Δf at $\Delta f/\Delta f_{\text{rt}}$ (to nearest integer) intervals. Uni directional irregular waves are thus defined and we now consider spread waves.

There are various options for generating directional waves, e.g. Latheef et al. (2017). The directional wave spectrum is usually defined by $S(f, \beta) = S(f) \cdot G(\beta)$ where the spreading function

$$G(\beta) = \alpha \left(\cos \frac{\beta}{2} \right)^{2s} \tag{34}$$

with the mean wave direction (heading) given by $\beta = 0$, for $-\pi < \beta < \pi$, and s is the spreading parameter. α is defined by the requirement $\int_{-\pi}^{\pi} G(\beta)d\beta = 1$. One approach for generating directional waves is to split each frequency component into directions defined by $G(\beta)$ known as the double summation method. However, this means that a specific frequency has several directional components and partial standing waves result; the wave field is non-ergodic (Jefferys 1987). To avoid this, each frequency component may be subdivided into a number of smaller components with different frequencies which together satisfy the spreading across the original frequency band, known as the single summation method. An equivalent more efficient approach, often

employed experimentally, is known as the random directional method (Latheef et al. 2017). The direction of propagation of any one frequency component is chosen randomly, subject to a weighting function based upon the desired directional spread. This approach also avoids components of the same frequency co-existing and results in ergodic wave fields. The appropriate weighting for choosing the direction of the components is based upon a normal distribution with a standard deviation of σ_β in accordance with the directional distribution

$$G(\beta) = \frac{\alpha}{\sigma_\beta \sqrt{2\pi}} \exp\left[-\frac{\beta^2}{2\sigma_\beta^2}\right], \tag{35}$$

where $\sigma_\beta^2 = \frac{2}{1+s}$ as a close approximation to Eq. (38) above. This is applied to each frequency component in the spectrum, as defined by the run time. The random angle is determined by the Box–Muller method where two random number numbers (u_1, u_2) are first generated from a uniform distribution between 0 and 1 and then converted to a random number:

$$u_3 = \sqrt{-2\ln(u_1)}\cos(2\pi u_2)$$

with unit standard deviation and mean zero, giving a random angle $u_3\sigma_\beta$. This is the approach adopted here to represent the effect of directional spread waves defined by the measured spectrum and a spread factor s.

The excitation forces and moments are affected by the heading angle and hydrodynamic (BEM) coefficients are determined at 2° intervals. The excitation forces and moments are as defined by Eq. (24) except that each frequency component k has a random heading from the normal distribution defined above, defining the excitation coefficients. This follows Stansby et al. (2022a)

6 Results

We assess the power capture and platform response in swell waves and choose a heading angle of zero for preliminary assessment. The hub acceleration is vital for reliable wind turbine operation, although wind speeds may be small in swell waves. With zero heading, the x acceleration is in line with the wave direction and greater than the y acceleration.

Passive dampers with $B_{mech} = 2 \times 10^9$ Nms/rad were found to give close to optimum average power and have been used throughout, although power is only slightly sensitive to this value. The dependence of average power on a wide range of B_{mech} is shown in Fig. 4 for swell waves with $T_p = 12$ s and $H_s = 2$ m at zero heading. The small horizontal stiffness constant k_s for station keeping was generally 5×10^5 N/m, although the results were insensitive to increasing by factor 10.

The floats have circular cross section but flat bases, which will generate some wake effects. The effect of drag coefficient C_d on mean power is shown in Fig. 5. With $C_d = 1$, the average power is about 17% smaller than with the inviscid value $C_d = 0$. $C_d = 1$ is used as a representative value.

Figure 6 shows the hub x acceleration dependence on T_p for $H_s = 2$ m with uni directional waves.

For swell waves ($T_p > 10$ s), the hub acceleration is greatest with a maximum of about 1.3 m/s² around $T_p = 12$ s. This is well below the operational limit of 3 m/s² and rms values are generally about a factor of 4 below the maxima. We next show the average power variation with T_p for the same conditions in Fig. 7. The maximum of about 270 kW occurs with $T_p = 12$ and 13 s where the energy wavelength (based on the energy period) is about 160 m, so the bow and stern floats with spacing of 80 m experience surge forces predominantly in anti-phase. The peak to mean power ratio is generally around 10. We have not considered the effect of wind as we only consider swell waves in low wind.

Uni directional waves rarely occur outside the laboratory and Fig. 8 shows the variation of average power with standard deviation σ of spread angle for $H_s = 2$ m and $T_p = 12$ s at zero heading.

There is a small drop in power due to spread which is only slightly dependent on spread angle. The variation of hub accelerations in the x and y directions with heading are shown in Fig. 9 for uni directional waves. The results show anti-symmetry as expected, e.g. for 0° and 90° and −90° and 180° where values for x and y directions swap.

Finally, we show the average power variation with heading in Fig. 10 for $T_p = 10$ and 12 s.

It can be seen that power is greatest between headings of 0° and 100°. Since swell waves come from a prevalent range of directions, usually around westerly, moorings can be arranged so that the platform is suitably oriented. The pitch angular motion of the supporting wind platform is of interest for access and maintenance purposes and Fig. 11 shows rotations θ about the y and x axes. The rms angles are about 0.8° while the maxima are about 2.7°. The relative pitch angles between the wave floats and the wind platform which generate power are shown in Fig. 12 to be somewhat larger with maxima over 4° corresponding with headings for maximum power, while the maximum rms values are 1.2°.

With the hinge almost rigid the hub accelerations are increased, the rms and maximum by 36%. This is counter-intuitive, as one might expect larger rigid bodies to respond less.

Results for different heading with a large $H_s = 6$ m and $T_p = 12$ s are shown without mechanical damping: in Fig. 13 for wind platform pitch angle, in Fig. 14 for relative pitch angle θ between wind platform and wave float, and in Fig. 15 for the rms and maximum hub accelerations. For these wave conditions, wind speed is likely to be above rated, but wind

Fig. 4 Variation of average power with mechanical damping B_{mech} for $T_p = 12$ s and $H_s = 2$ m at zero heading
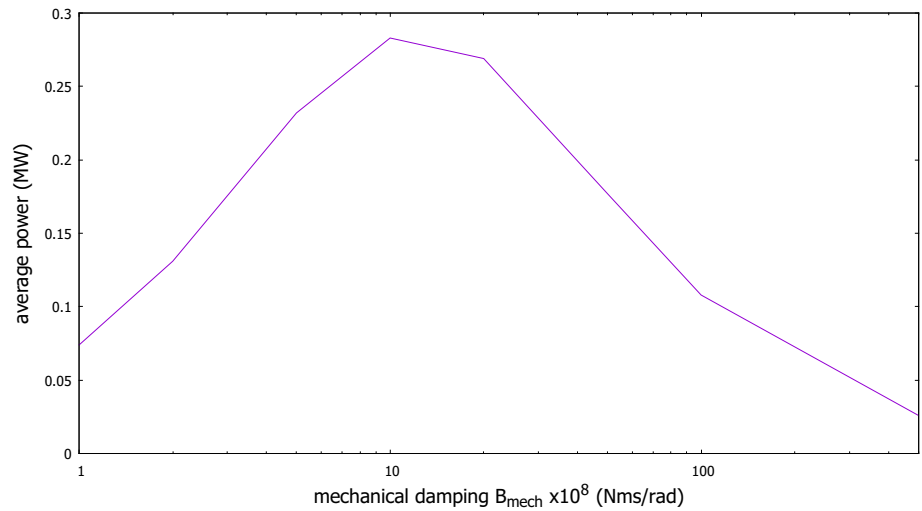

Fig. 5 Variation of average power with C_d for $T_p = 12$ s and $H_s = 2$ m at zero heading
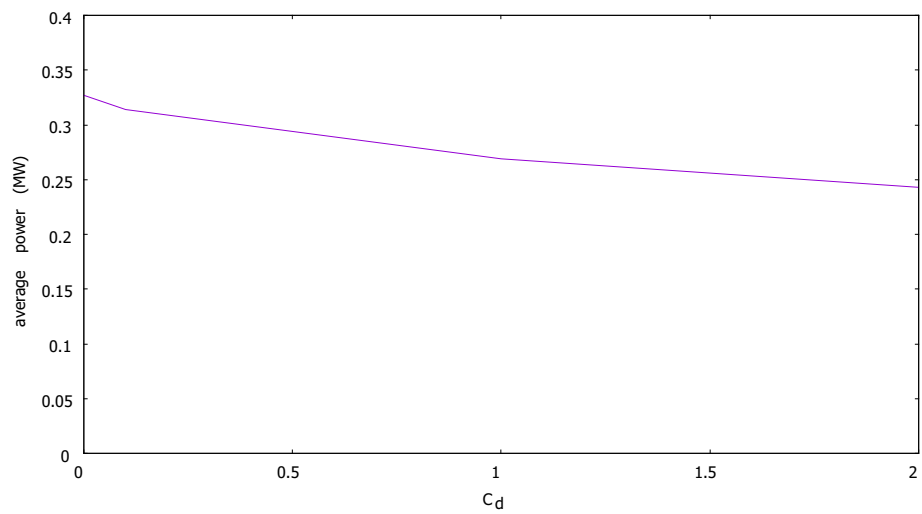

Fig. 6 Variation of hub acceleration in x direction with T_p for $H_s = 2$ m with uni directional waves at zero heading
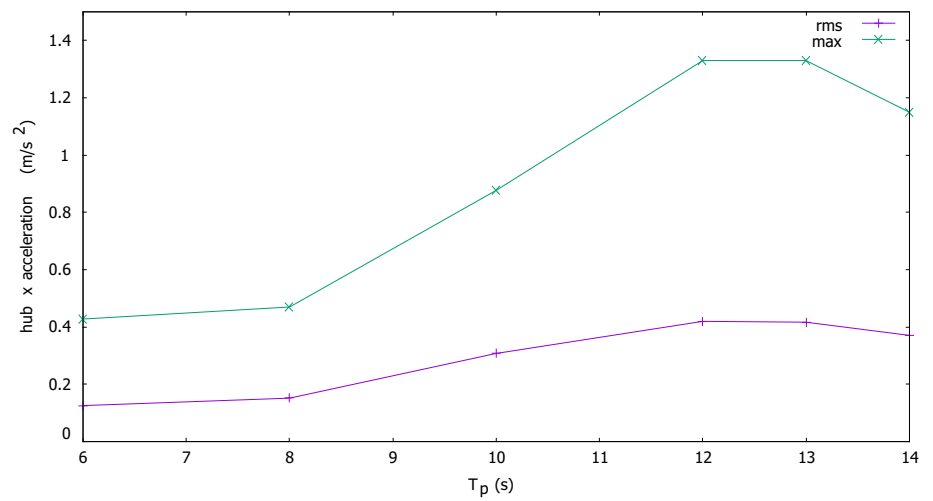
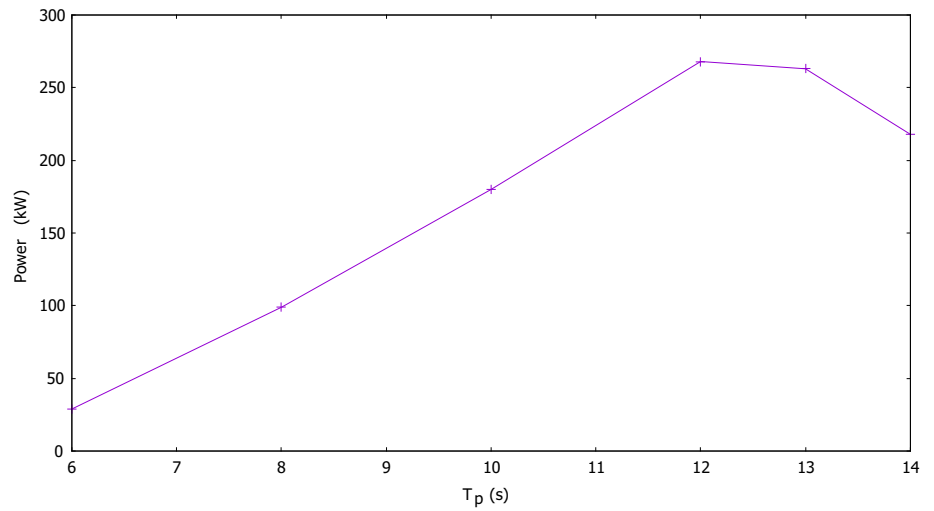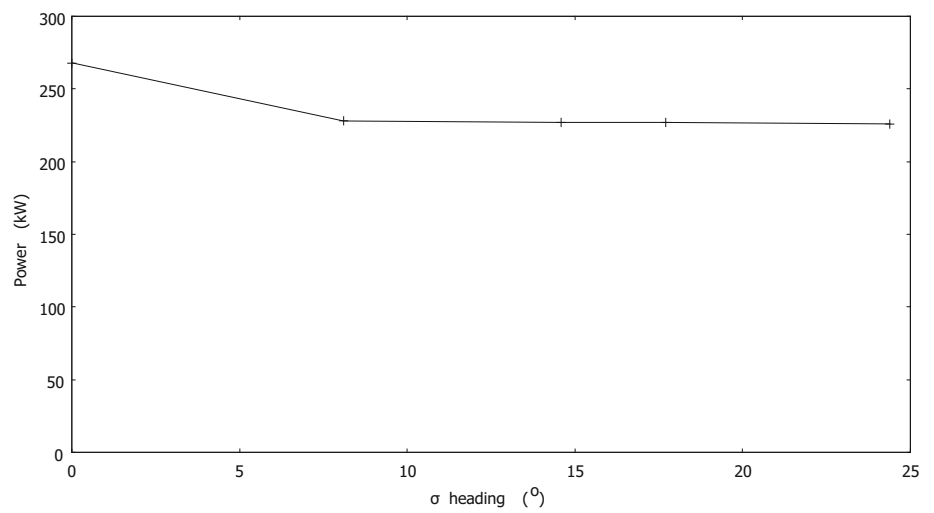**Fig. 7** Variation of average power with T_p for $H_s = 2$ m with uni directional waves

Fig. 8 Variation of average power with standard deviation σ of spread angle for $H_s = 2$ m and $T_p = 12$ s at zero heading

Fig. 9 Variation of rms and maximum hub accelerations in the x and y directions with heading for uni directional waves with $H_s = 2$ m and $T_p = 12$ s with power take off
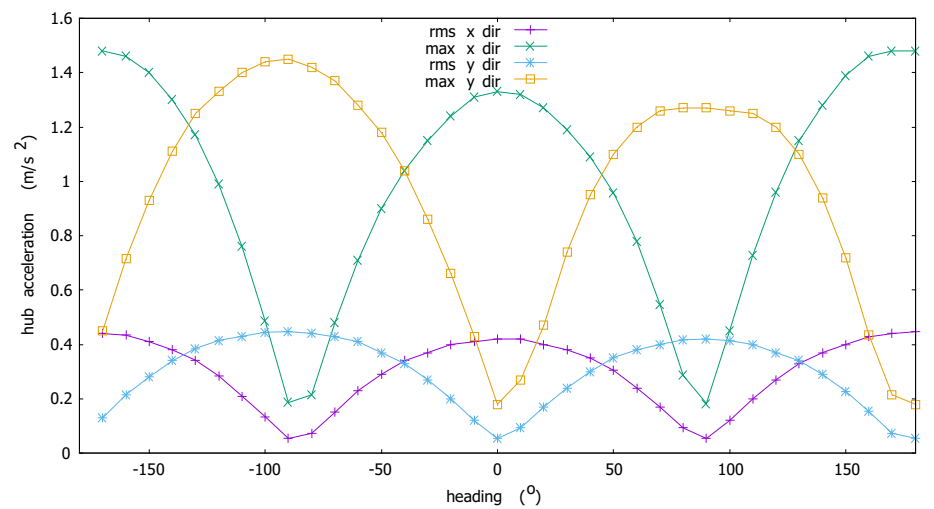
Fig. 10 Variation of average power with heading for $T_p = 10$ and 12 s with $H_s = 2$ m for uni directional waves
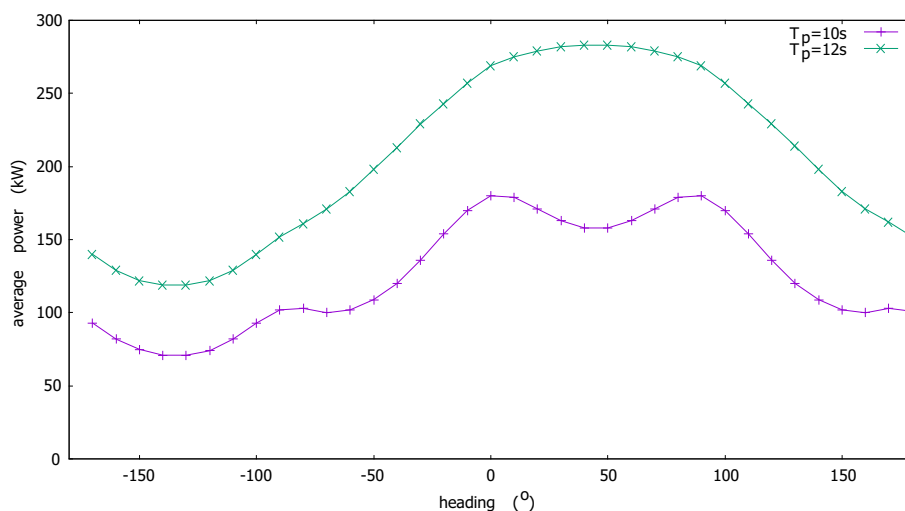
Fig. 11 Variation of wind platform pitch angle θ about the x and y axes variation with heading for uni directional waves with $H_s = 2$ m and $T_p = 12$ s with PTO
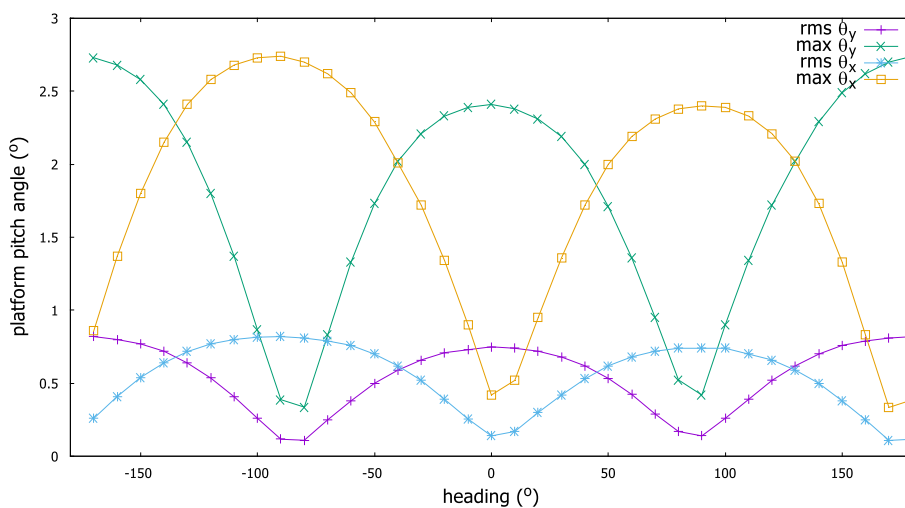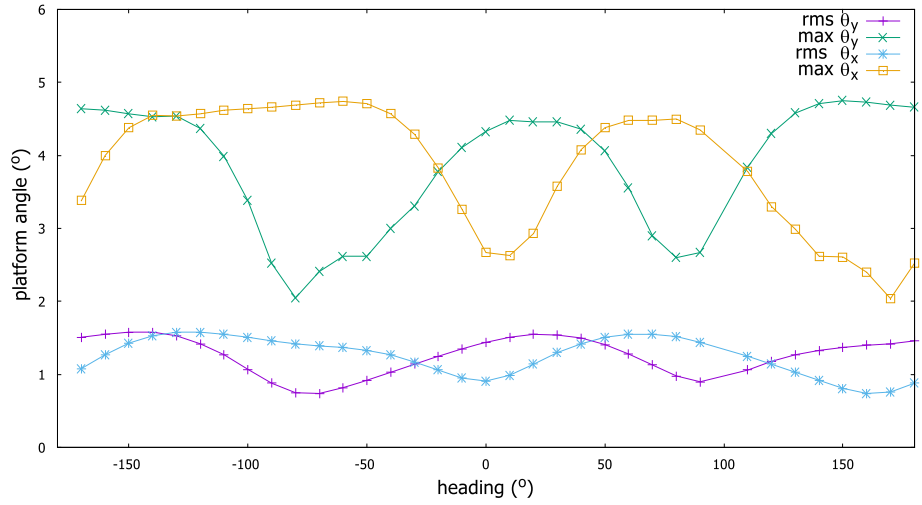

Fig. 12 Variation of the relative pitch angle θ between the wind platform and wave floats about the x and y axes with heading for uni directional waves with $H_s = 2$ m and $T_p = 12$ s with PTO
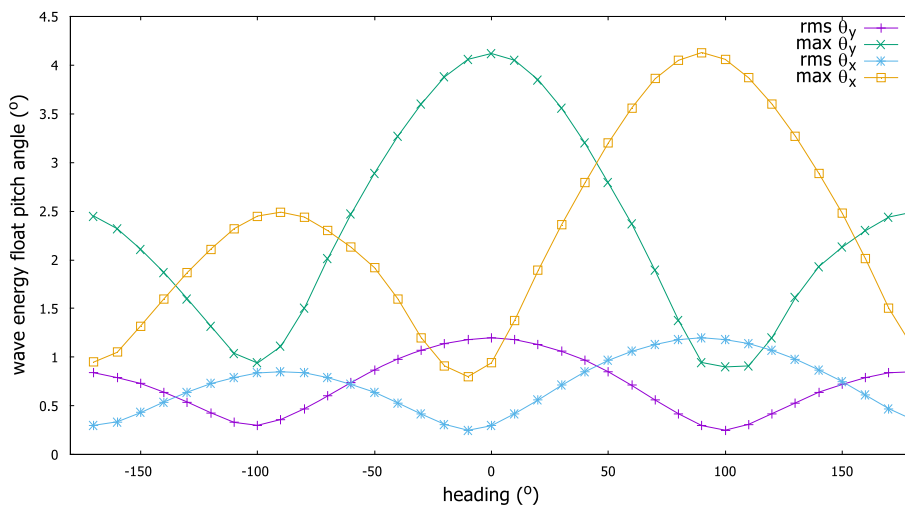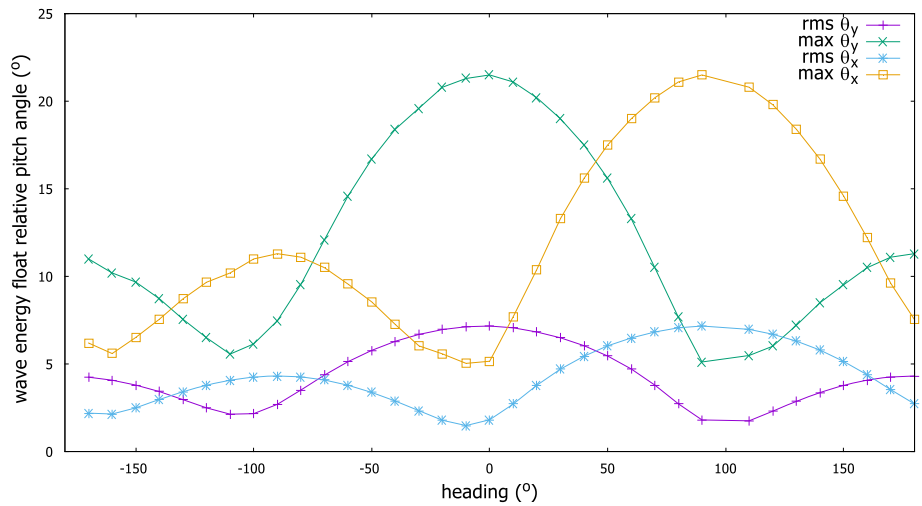
Fig. 13 Variation of wind platform pitch angle θ about the x and y axes variation with heading for uni directional waves with $H_s = 6$ m and $T_p = 12$ s with no PTO

Fig. 14 Variation of the relative pitch angle θ between the wind platform and wave floats about the x and y axes with heading for uni directional waves with $H_s = 6$ m and $T_p = 12$ s with no PTO

Fig. 15 Variation of rms and maximum hub accelerations in the x and y directions with heading for uni directional waves with $H_s = 6$ m and $T_p = 12$ s with no PTO and no wind
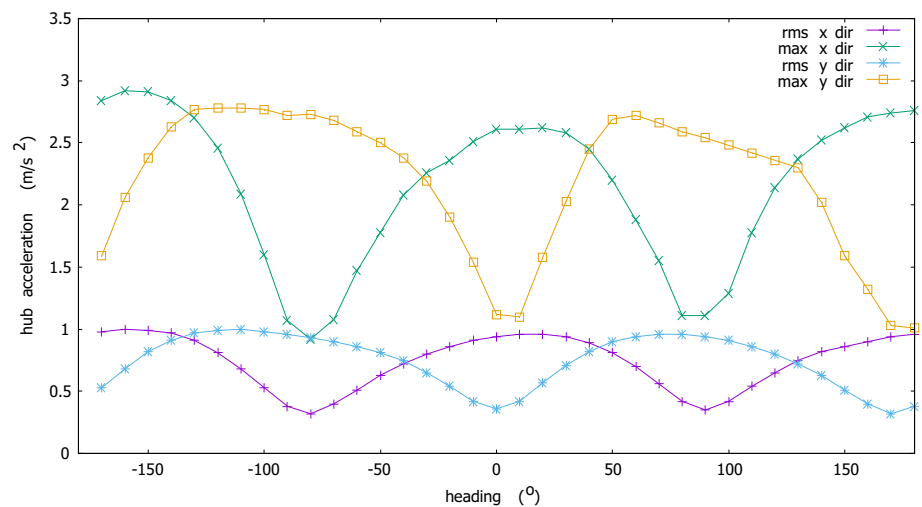
effect is not included as this will be seen to slightly reduce motion. The wind platform angles are small, with maxima of about 4½° and rms of 1½°. In contrast, the relative angles are quite large with the largest maxima of 22° and rms of about 8°. The greatest hub accelerations are just less than 3 m/s^2 and rms are about 1 m/s^2. With the wave float connection made effectively rigid, the rms is increased by 64% and the maximum by 87% with zero heading. This is consistent with the result for $H_s = 2$ m with PTO engaged where a smaller increase resulted. It should be noted that in extreme steep waves, the wave floats will be intermittently overtopped and partially submerged based on experience for the multi-float wave energy converter M4, limiting the pitch motion and providing a passive end stop to rotation, e.g. Stansby et al. (2022b), and this is obviously not captured in a linear wave diffraction–radiation model.

The effect of spread on hub acceleration is shown in Fig. 16 for the x direction only. In general, spread slightly reduces rms acceleration, but can slightly increase maximum values which is unexpected.

Finally, we consider the effect of wind in line with zero heading. The effect on hub acceleration with speeds up to 25 m/s was small with maximum 6% reduction at about 10 m/s, close to rated, tested with $H_s = 6$ m (without PTO). There was a maximum 13% reduction in wave power with $H_s = 2$ m at this wind speed. Some reduction is to be expected as an oscillating turbine provides damping.

7 Discussion

The model is based on linear diffraction–radiation theory which is strictly limited to small wave heights and response. Similar multi-float configurations have been compared with experiment for both M4 wave energy generation (Stansby and Carpintero Moreno 2020; Stansby and Draycott 2024) and a floating wind platform with damping plates (Stansby et al. 2019) using a single point mooring buoy and have shown good agreement for response in operational and also in steep waves. Experimental analysis for M4 in focussed waves has also shown response to be remarkably linear in large waves with weak higher-order effects (Santo et al. 2017). Measured mooring forces were, however, highly nonlinear (Stansby et al. 2019, 2022b), but not considered here where a small spring stiffness is added in the horizontal directions for station keeping. In large steep waves, the float decks were intermittently overtopped and partially submerged causing sloshing and energy dissipation, capping the pitch motion, acting as an end stop (Stansby et al. 2022b). In these cases, the wave PTO is disengaged. This will also occur for the hybrid wind–wave platform considered here. The angular response was effectively decoupled from the mooring forces, but this may be affected by moorings if attached directly to the wind

floats. The results for response and power are thus expected to be realistic while nonlinear analysis and experimentation will eventually be desirable particularly in relation to drag effects with sharp corners. A representative drag coefficient is used here and results have been shown to be relatively insensitive to its value for this configuration between 0 and 2.

The aim is to generate power from swell waves when wind power is negligible while preferably reducing platform pitch and hence hub acceleration in larger waves. Swell has periods larger than about 10 s and heave resonance would require impractically large drafts where wave excitation on the base would be small. However, with distance between wind floats (with 3 floats forming an effectively rigid body) and wave floats of about half a wavelength, the excitation forces are approximately in anti-phase generating an oscillatory moment about the hinge points. Significant swell wave power is generated between 10 and 14 s with headings over a 100° range. The effect of wave spread is relatively small. Also with insensitivity to drag coefficient, there is little advantage in having hemi-spherical or rounded bases to reduce drag as found desirable for wave energy converters in wind waves of smaller periods (Stansby et al. 2017). For this application, wind power exceeds swell wave power with wind speeds above about 5 m/s. A flat float base is desirable for ease of fabrication.

The response between wave floats is strongly coupled, e.g. with zero heading and PTO engaged, the relative angular motion in roll is 25% of that for pitch, although the corresponding wave power due to roll is 8% of that due to pitch. Without the PTO engaged for the wind floats, the roll motion is 63% of the pitch motion, while the relative roll motion is still 25% of pitch motion. This complex cross coupling must cause the rotational wind platform motions in both directions to be relatively small, which is desirable. The relative rotation with the wave floats is larger and power generation requires very high torques at low rotational speeds. This raises the question of when to disengage the power take-off. Clearly, there is no point in generating wave power when wind power is far greater. When to disengage depends on the combination of swell wave height and wind speed and is site specific; this is not analysed here.

The three-float wind platform pitch response without the PTO engaged in large waves is quite small, with rms of 1.5° and maxima of about 4.5° with $H_s = 6$ m and $T_p = 12$ s. Importantly, this causes the hub accelerations to be less than 3 m/s^2 and this will be reduced slightly with wind damping. The maximum relative angular response, however, is about 22°. With the five floats acting almost as a rigid body, the wind pitch is increased markedly by about 120% and the maximum hub acceleration by 87%. This is counterintuitive, as one generally expects larger bodies to respond less. It does mean that the wave floats have a beneficial effect on the wind floats in

Fig. 16 Variation of rms and maximum hub accelerations in the x direction with heading for uni directional and spread waves ($s = 20$, $\sigma = 17.7°$) with $H_s = 6$ m and $T_p = 12$ s with no PTO and no wind
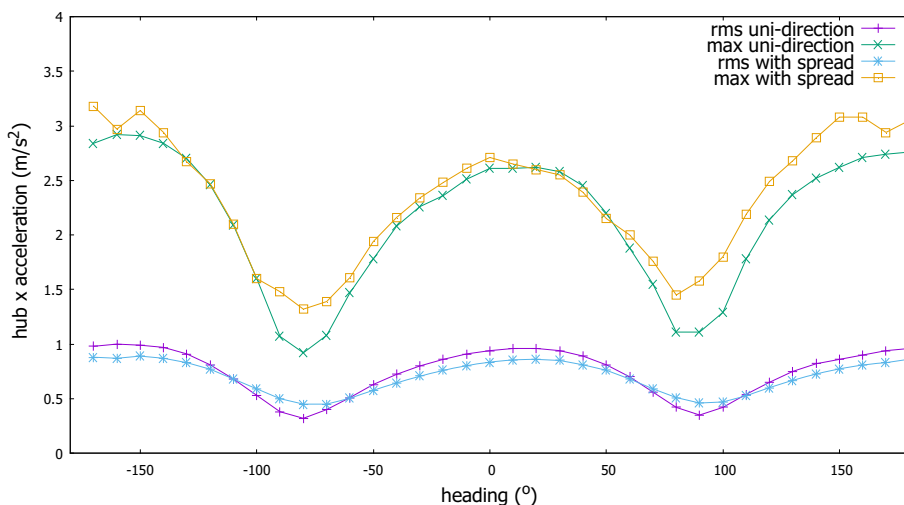
large waves with the PTO disengaged, although this will be modified by intermittent float overtopping and submergence which requires experimental investigation. Damping plates may be added to the wind floats to reduce motion further, but this may reduce wave power generation in low wind conditions. Control of motion by pumping water between wind floats to reduce pitch may also be beneficial in large waves while switched off for swell wave generation.

The dimensions and spacing of the floats were chosen to be similar to Windfloat with sufficient buoyancy to support the wind turbine and column and WEC PTOs. The spacing between fore and aft floats is close to half the energy wavelength with $T_p = 12$ s, but the length of wave float beam may be adjusted to suit most likely swell wave conditions. Clearly, there is scope for optimisation of dimensions, which will be site specific. There is also scope for the torque control to optimise swell wave power generation which would be expected to increase the average power by up to 100% for long wave periods (Liao et al. 2020, 2021). Control to minimise response in combination with maximising power is probably not necessary, as response is small in swell waves and power is disengaged in large waves.

It is possible to make some comparison with other hybrid systems. The system with torus absorbers on four columns gave 400 kW mean power in regular waves with 2 m height (Tian et al. 2023), which is approximately equivalent to 200 kW in irregular waves with $H_s = 2$ m, similar to that produced here; however, this increased pitch motion in swell waves. The addition of three outer floats to the three-float DeepCwind platform generated 180 kW with $H_s = 2.5$ m and $T_p = 10$ s and reactive control (Si et al. 2021) which is equivalent to 115 kW with $H_s = 2$ m. Adding heaving point absorbers between the upper and lower connecting beams of a Windfloat-type platform gave an average power of 300 kW in regular waves with height of 2 m (Hu et al. 2020), equivalent

to 150 kW in irregular waves with $H_s = 2$ m. The magnitudes of wave power generated are thus generally similar in the range 100–200 kW, although the effect on pitch angle is quite uncertain. In the present configuration, the magnitudes of power in swell are slightly larger and would be increased further by control. There is the advantage that wind platform pitch is reduced in large waves, but with quite large relative pitch motions, e.g. 22° with $H_s = 6$ m. In practice, the extent of pitch motion is limited by overtopping of the wave floats, to about 40° for a wave energy converter (Stansby and Carpintero Moreno 2020; Stansby et al. 2022b).

It is apparent that the economic benefit of such a wind–wave platform is dependent on many factors, including the wind and wave climate for a potential site. The wave PTOs will be an additional cost; the storage required for continuity of supply will be reduced; wave PTO control will increase wave energy capture; the upper wind speed limit for wind power generation will be increased as disengaged wave floats reduce wind float pitch and hence hub acceleration. The platform cost is thus effectively increased by the two wave PTOs with hinges and the question is whether there is a cost benefit from the additional wave and wind energy generation. There is the additional consideration that the spot price of electricity is higher in low wind conditions when the ever-present swell wave energy would have an above average value.

Finally, it is useful to compare with a platform used only for wave energy conversion. The three-float M4 device was designed with a hydraulic PTO for Leixoes, Portugal, with a most likely wave condition of $H_s = 2.3$ m and $T_p = 13$ s giving an average power of 840 kW (Gaspar et al. 2021). With four PTOs, power is approximately quadrupled to 3.4 MW (Liao et al. 2021) with capacity of say 10 MW. In due course, this may be a viable alternative to wind or hybrid wind–wave platforms.

8 Conclusions

The aim of the hybrid concept is to generate wave energy on a semi-sub wind platform from the almost ever present swell waves, important when wind speed is too low to generate wind power. This naturally improves uniformity of supply and reduces the need for storage of wind energy. With swell periods over 10 s, heave resonance is difficult to achieve, but pitch resonance may be achieved with the fore and aft floats about half a wavelength apart with anti-phase forcing causing pitch moment on hinges above water level. Importantly significant wave power occurs for omnidirectional headings over a range of about 100°. With $H_s = 2$ m, the average power is over 200 kW with an optimised passive damper and this may be improved by control. In large waves and generally strong winds, with wave power disengaged, wind float pitch and hence hub accelerations are reduced potentially enabling longer times before shutdown due to the hub acceleration limit, typically 3 m/s^2. The intention here is to demonstrate the platform concept for swell waves. Designs would need to be optimised for a given ocean wind and wave climate, taking account of materials, fabrication and moorings.

Declarations

Competing interests The authors declare no competing interests.

References

Apsley DD, Stansby PK (2020) Unsteady thrust on an oscillating wind turbine: comparison of blade-element momentum theory with actuator-line CFD. J Fluids Struct 98:103141

Arinaga RA, Cheung KF (2012) Atlas of global wave energy from 10 years of reanalysis and hindcast data. Renew Energy 39:49–64

Carbon Trust (2015) Floating offshore wind: market and technology review. Report for the Scottish Government

De Souza CES, Bachynski-Polić EE (2022) Design, structural modeling, control, and performance of 20 MW spar floating wind turbines. Mar Struct 84:103182

Fath A, Yazdi EA, Eghtesad M (2020) Semi-active vibration control of a semi-submersible offshore wind turbine using a tuned liquid multi-column damper. J Ocean Eng Mar Energy 6:243–262

Gaspar JF, Stansby PK, Calvario M, Guedes Soares C (2021) Hydraulic power take-off concept for the M4 wave energy converter. Appl Ocean Res 106:102462

Hu J, Zhou B, Vogel C, Liu P, Willden R, Sun K, Zang J, Geng J, Jin P, Cui L, Jiang B, Collu M (2020) Optimal design and performance analysis of a hybrid system combing a floating wind platform and wave energy converters. Appl Energy 269:114998

Jefferys E (1987) Directional seas should be ergodic. Appl Ocean Res 9(4):186–191

Kamarlouei M, Gaspar JF, Calvario M, Hallak TS, Mendes MJGC, Thiebaut F, Guedes Soares C (2022) Experimental study of wave energy converter arrays adapted to a semi-submersible wind platform. Renew Energy 188:145–163

Kluger JM, Haji MN, Slocum AH (2023) The power balancing benefits of wave energy converters in offshore wind–wave farms with energy storage. Appl Energy 331:120389

Latheef M, Swan C, Spinneken J (2017) A laboratory study of nonlinear changes in the directionality of extreme seas. Proc Roy Soc A 473:20160290

Li GQ, Stansby PK (2023) Software framework to accelerate BEM linear wave load program using OpenMP (OREGEN-BEM). ISOPE Conference, Ottawa

Li L, Gao Y, Yuan Z, Day S, Hu Z (2018) Dynamic response and power production of a floating integrated wind, wave and tidal energy system. Renew Energy 116:412–422

Liao Z, Stansby P, Li G (2020) A generic linear non-causal optimal control framework integrated with wave excitation force prediction for multi-mode wave energy converters with application to M4. Appl Ocean Res 97:102056

Liao Z, Stansby P, Li G, Carpintero Moreno E (2021) High-capacity wave energy conversion by multi-floats, multi-PTO, control and prediction: generalised state-space modelling with linear optimal control and arbitrary headings. IEEE Trans Sustain Energy 12(4):2123–2131

Michailides C, Gao Z, Moan T (2016) Experimental study of the functionality of a semisubmersible wind turbine combined with flap-type wave energy converters. Renew Energy 93:675–690

Ren N, Ma Z, Shan B, Ning D, Ou J (2020) Experimental and numerical study of dynamic responses of a new combined TLP type floating wind turbine and a wave energy converter under operational conditions. Renew Energy 151:966–974

Robertson AN et al (2017) OC5 Project Phase II: validation of global loads of the DeepCwind floating semi-submersible wind turbine. Energy Procedia 137:38–57

Roddier D, Cermelli C, Aubault A, Weinstein A (2010) WindFloat: a floating foundation for offshore wind turbines. J Renew Sust En 2:033104

Santo H, Taylor PH, Carpintero Moreno E, Stansby P, Eatock Taylor R, Sun L, Zang J (2017) Extreme motion and response statistics for survival of the three-float wave energy converter M4 in intermediate water depth. J Fluid Mech 81:175–204

Si Y, Chen Z, Zeng W, Sun J, Zhang D, Ma X, Qian P (2021) The influence of power-take-off control on the dynamic response and power output of combined semi-submersible floating wind turbine and point-absorber wave energy converters. Ocean Eng 227:108835

Stansby PK (2021) Reduction of wave-induced pitch motion of a semi-sub wind platform by balancing heave excitation with pumping between floats. J Ocean Eng Mar Energy 7:157–172

Stansby PK, Carpintero Moreno E (2020) Hydrodynamics of the multi-float wave energy converter M4 with slack moorings: time domain

linear diffraction–radiation modelling with mean force and experimental comparison. Appl Ocean Res 97:102070

Stansby P, Draycott S (2024) M4 WEC development and wave basin Froude testing. Eur J Mech-B/fluids 104:182–193

Stansby P, Carpintero Moreno E, Stallard T (2017) Large capacity multi-float configurations for the wave energy converter M4 using a time domain linear diffraction model. Appl Ocean Res 68:53–64

Stansby PK, Carpintero Moreno E, Apsley DD, Stallard TJ (2019) Slack-moored semi-submersible wind floater with damping plates in waves: linear diffraction modelling with mean forces and experiments. J Fluids Struct 90:410–431

Stansby PK, Carpintero Moreno E, Draycott S, Stallard T (2022a) Total wave power absorption by a multi-float wave energy converter and a semi-submersible wind platform with a fast far field model for arrays. J Ocean Eng Mar Energy 8:43–63

Stansby P, Draycott S, Li GQ, Zhao C, Moreno EC, Pillai A, Johanning L (2022b) Experimental study of mooring forces on the multi-float WEC M4 in large waves with buoy and elastic cables. Ocean Eng 266:113049

Tian W, Wang Y, Shi W, Michailides C, Wan L, Chen M (2023) Numerical study of hydrodynamic responses for a combined concept of semisubmersible wind turbine and different layouts of a wave energy converter. Ocean Eng 272:113824